nature communications

Article

https://doi.org/10.1038/s41467-025-64409-8

Multicolor cathodoluminescence imaging of single lanthanide nanoparticles

Received: 21 August 2024

Accepted: 15 September 2025

Published online: 31 October 2025

Check for updates

Sohaib Abdul Rehman[1,2,4], Jeremy B. Conway[1,2,4], Amy Nichols[1,2], Edward R. Soucy[3], Amanda Dee[1,2], Kristal Stevens[1,2], Simon Merminod[1,2], Isabella MacNaughton[1,2], Abigail Curtis[1,2] & Maxim B. Prigozhin[1,2]

Cathodoluminescence (CL) microscopy offers a promising approach to nanoscale analysis, enabling detection of optical emission from a sample while leveraging the high resolution of electron microscopy. However, achieving multicolor single-particle CL imaging remains a significant challenge. Here, using lanthanide nanoparticles as a model system, we identify a critical limitation in CL imaging: nonlocal signal caused by stray electrons. We mitigate these nonlocal excitations and demonstrate multicolor single-particle CL imaging of nanoparticles down to 12 nm in diameter. Using this enhanced sensitivity, we demonstrate that CL brightness increases monotonically with nanoparticle diameter. We propose that multicolor imaging of spectrally distinct nanoparticles in the same field of view, coupled with the scaling of CL brightness with nanoparticle size, is crucial for confirming single-particle CL detection. Finally, we demonstrate the utility of our findings by imaging lanthanide nanoparticles in a biological sample. This work advances our understanding of nanoscale photonic responses to free electrons, establishing CL as a useful contrast mechanism for high-resolution, multicolor electron microscopy.

Local nanoscale probing of optical properties is essential for high-resolution analysis of samples across various scientific disciplines. In cell biology, nanoscale imaging can reveal the localization of biomolecules and report on local chemical environments[1–3]. In materials science, optical properties offer information about electronic structure, energy transfer and relaxation pathways, exciton migration dynamics, phonon modes, and plasmonic nanostructures[4–9]. These properties are typically investigated through photoluminescence, in which photon emission is induced by optical excitation. However, the resolution of far-field photoluminescence imaging is fundamentally restricted by the diffraction of light, which constrains the diameter of the excited region to >250 nm when exciting in the visible spectral range. Unfortunately, this length scale is over an order of magnitude larger than the nanometer dimensions at which biomolecules are typically localized and interact, and where intriguing optical properties of materials need to be examined.

To address this mismatch between the optical resolution limit and the nanoscale features of interest, several strategies that overcome the diffraction barrier have been developed. For instance, in near-field microscopy, nanoscale optical excitation is achieved by scanning a sub-wavelength-sized probe close to the sample surface[10]. Despite its nanoscale resolution, this method is restricted to the sample surface, suffers from slow imaging speed, and involves complex instrumentation. On the other hand, super-resolution fluorescence microscopy methods achieve nanoscale resolution using specialized photoluminescent probes whose fluorescence can be activated and deactivated within the diffraction-limited excitation regions[11–15]. However, these techniques are limited to fluorescence imaging applications where such control over probe behavior is possible and are not broadly

[1]Department of Molecular and Cellular Biology, Harvard University, Cambridge, MA, USA. [2]John A. Paulson School of Engineering and Applied Sciences, Harvard University, Cambridge, MA, USA. [3]Center for Brain Science, Harvard University, Cambridge, MA, USA. [4]These authors contributed equally: Sohaib Abdul Rehman, Jeremy B. Conway. e-mail: maxim_prigozhin@harvard.edu

applicable to study the intrinsic optical properties of arbitrary materials.

Alternatively, an electron beam can produce luminescence in a material through an electron-matter-light interaction known as cathodoluminescence (CL)[16]. CL is a contrast mechanism that can reveal generalizable insights into the photonic response of materials to free electrons. The short wavelength of electrons enables nanoscale focusing of the electron beam, which, combined with fast beam scanning, allows precise, localized optical excitation in the far-field regime. As a result, despite the optical nature of CL emission, it can retain the resolving power of electron microscopy (EM). In addition, CL contrast reveals the nanoscale optical properties of materials, which distinguishes it from other spectroscopic EM methods like electron energy loss spectroscopy (EELS) and energy-dispersive X-ray analysis (EDX), which focus on electron energy losses or X-rays generated during electron-matter interactions, respectively, and are primarily used for elemental analysis[17,18].

The interaction of free electrons with the specimen can excite CL across the entire visible spectrum[19]. This broadband excitation, combined with nanoscale spatial resolution, makes CL a versatile tool with diverse applications. For example, in materials science, CL could probe nanoscale defects and band structures of semiconductors[20,21]. In quantum information science, CL would enable local excitation of electron-hole pairs in quantum systems at the scale of their wavefunction[22–24]. In geosciences, CL is already used for mineral identification, structural studies, and geochronology[25]. Moreover, since CL imaging is performed within an electron microscope, CL signals are acquired in parallel with electron-scattering-based images, which provides additional structural and morphological context. In biological imaging, this multimodal approach bridges optical and electron microscopy by enabling nanoscale molecular localization via CL contrast, as well as imaging of cellular ultrastructure (such as membranes, chromatin, and the cytoskeleton) via electron contrast, offering an attractive alternative to correlative light and electron microscopy (CLEM)[26,27].

However, despite its potential, the underlying imaging physics of CL remains poorly understood, limiting applications of CL in nanoscale imaging. We illustrate this point using lanthanide nanoparticles (LNPs) that serve as a prototypical model system to study CL imaging. LNPs are nanocrystals doped with ions from the lanthanide series (see Supplementary Figs. 2–4 for TEM images of the LNPs). The electronic structure of a lanthanide ion determines the nanoparticle's CL emission spectrum[28]. These nanoparticles exhibit exceptional photostability due to the independent emission of each dopant ion within their volume, preventing single-step photobleaching[29]. LNPs also offer precise synthetic control over morphology and composition, allowing the investigation of size-dependent properties and generation of a multicolor palette of nanocrystals with distinct, sharp emission bands[30]. These spectral features facilitate spectral isolation of CL signals and multiplexing for imaging applications. In addition, due to the high atomic numbers of their constituent ions, single LNPs are clearly visible in scanning electron microscopy (SEM), making this system highly tractable in CL imaging.

Previous research on CL imaging has focused on small nanocrystals (10–30 nm), which are promising for studying size-dependent luminescence at the scale of the electron-sample interaction volume and as nanoprobes for biological imaging[27]. However, multicolor CL imaging of individual nanoparticles within one field of view remains elusive. Prior studies have been limited to single-color imaging[28,31–35] or multicolor imaging of large nanoparticles or aggregates (>100 nm in size)[36–38]. In addition, challenges persist in distinguishing CL signals from different nanoparticles in the same field of view, achieving reproducible single-particle CL intensity measurements, and establishing clear correlations between CL intensity and nanoparticle size[28,34].

Here, we identify a critical limitation in achieving single-particle sensitivity in CL measurements: the nonlocal CL signal caused by stray electrons. This phenomenon hinders single-particle imaging, limiting our understanding of the nanoscale photonic response of materials to free electrons. We investigate the origin and extent of these nonlocal excitations and their impact on CL imaging. We also identify sample preparation and imaging conditions to mitigate this nonlocal signal and enable single-particle detection. By leveraging this sensitivity, we establish a linear dependence of CL emission rate on LNP diameter, which is supported by Monte Carlo simulations of electron trajectories. We conclude that both monotonic scaling of CL rate with LNP size and multicolor imaging of spectrally distinct LNPs in the same field of view are essential for demonstrating single-particle CL detection. We further show single-particle imaging capabilities in biological samples by imaging LNPs on the surface of mammalian cells. These results demonstrate the versatility of single-particle CL imaging across different systems.

Results

Nonlocal excitation prohibits single-particle CL imaging

CL imaging was performed in SEM using a custom parabolic mirror and an optical detection system to collect CL (Supplementary Fig. 6). In our initial experiments to characterize the CL signal from lanthanide ions, we imaged single LNPs in samples containing LNPs doped with a single type of lanthanide ion. As expected, these LNPs predominantly emitted in the spectral channels corresponding to the primary emission peaks of the constituent ion, as shown in Fig. 1a for $NaHoF_4$ and $NaDyF_4$ LNPs. For simplicity, we refer to these color channels according to the lanthanide ion associated with the dominant peak detected in the channel (e.g., Ho^{3+} channel and Dy^{3+} channel). However, in these experiments, despite the apparent spectral stability of single LNPs and the spatial resolution of CL images closely matching the SEM images, we observed an unexpected result: the CL from LNPs was not monotonically correlated with their size (Fig. 1b). This finding, though consistent with previous results[28,34], was puzzling because we expected the brightness of LNPs to increase as a function of their size, as larger LNPs would contain a greater number of excitable lanthanide ions—the color centers responsible for CL emission. Such a monotonic scaling has also been observed in optically addressable upconverting LNPs[39,40]. Moreover, this size independence was contrary to the predictions from our Monte Carlo electron trajectory simulations, which suggested a linear relationship between the nanoparticle size and the energy absorbed by LNPs (a proxy for CL signal[41]) at the 3 keV electron beam energy used in our experiments (Fig. 1c).

Another unexpected observation was made when we imaged single LNPs in mixed samples containing two different types of LNPs: $NaHoF_4$ and $NaDyF_4$. Despite imaging single LNPs doped with either Ho^{3+} or Dy^{3+} ions, but not both, we detected CL signal in both Ho^{3+} and Dy^{3+} color channels (Fig. 1d). In optical microscopy, such a result would be anomalous, as it would imply that a single fluorophore emits across two distinct spectral ranges. Therefore, we suspected an EM-specific phenomenon: nonlocal excitation of sample features (mainly LNP aggregates) that were present in the field of view of the parabolic mirror but were not directly excited by the primary electron beam. This hypothesized origin of the nonlocal CL signal is illustrated in Fig. 1e.

To investigate whether this nonlocal excitation of the sample was responsible for the observed crosstalk, we separated nanocrystals of two different colors on a Si wafer (total area: ≈1 cm^2). Half of the wafer was covered with a thick layer (>10 μm) of luminescent $NaDyF_4$ LNPs, while the other half of the wafer was coated with sparsely dispersed individual luminescent $NaHoF_4$ LNPs (Fig. 2a). When we imaged single $NaHoF_4$ LNPs located >200 μm away from the edge of the dense $NaDyF_4$ layer, no CL signal was observed in the Dy^{3+} channel. This result was expected because of the minimal spectral overlap between

https://doi.org/10.1038/s41467-025-64409-8

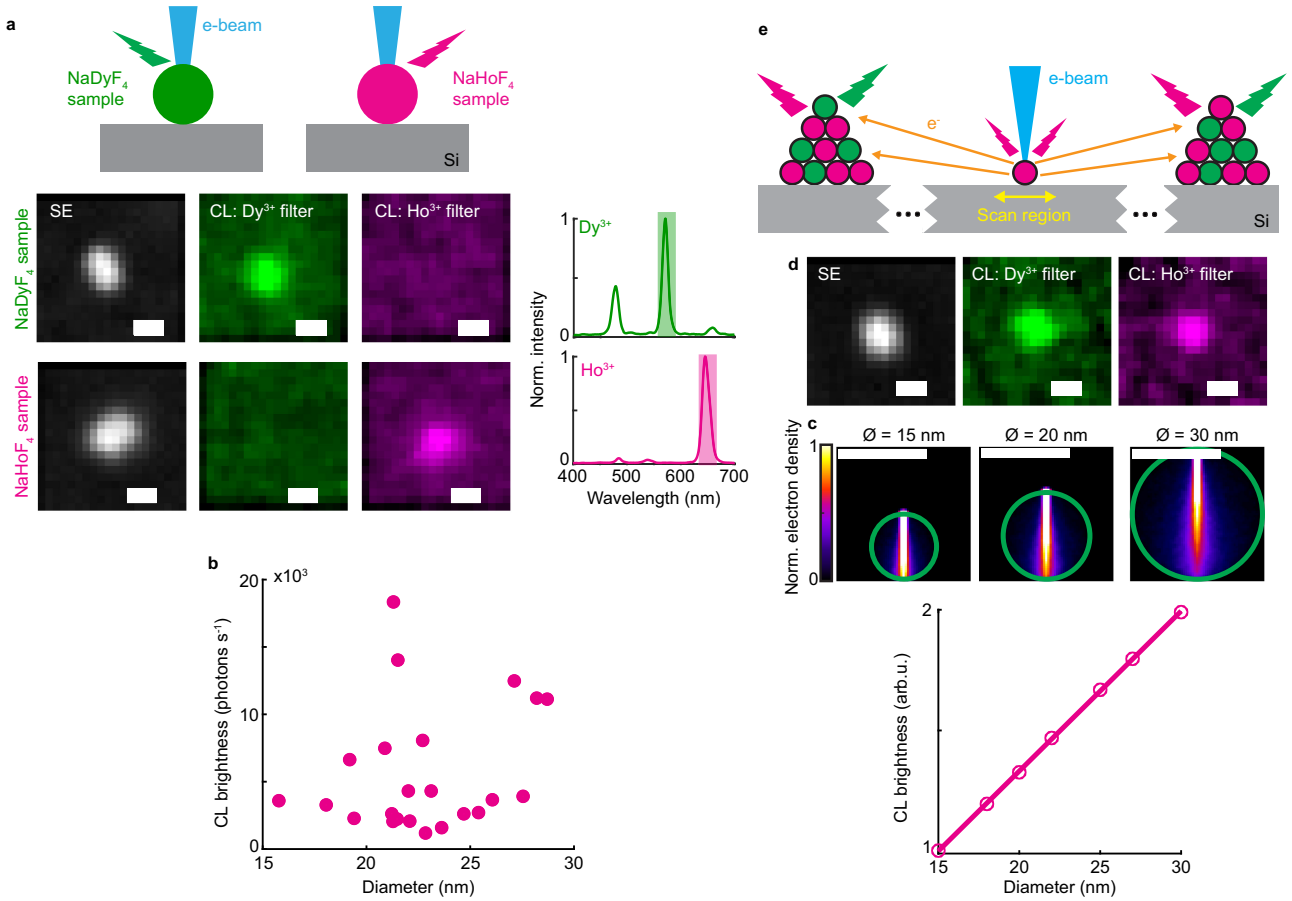

Fig. 1 | Challenges in achieving single-particle CL imaging at the nanoscale. **a** Secondary electron (SE) and CL signal collected from single LNPs in samples containing either $NaHoF_4$ or $NaDyF_4$ LNPs. Ensemble CL spectra of the LNPs and transmission bands of optical filters (shaded bands) used in CL imaging are also shown. **b** Observed brightness of $NaHoF_4$ LNPs as a function of their size. **c** Simulated dependence of CL signal on $NaHoF_4$ LNP size at 3 keV electron beam energy. Energy absorbed by the nanoparticles was used as a proxy for CL brightness. The interaction volume of the electron beam inside nanoparticles of different diameters (ø), 15, 20, and 30 nm, is also shown. Colormap shows the normalized electron density. **d** SE and CL signals collected from a single LNP in a sample containing both $NaHoF_4$ and $NaDyF_4$ LNPs. **e** Illustration showing the origin of nonlocal CL signal due to stray electrons originating from the excited LNP. Scale bars: **a**, **c**, **d** 20 nm. Pixel intensity scaling: **a** 300–1400 photons s^{-1}, **d** 300–800 photons s^{-1}. Source data are provided as a Source Data file.

$NaHoF_4$ emission and the Dy^{3+} channel (Supplementary Fig. 7). However, when we imaged $NaHoF_4$ LNPs located within 200 μm of the $NaDyF_4$ edge, an unexpected signal was detected in the Dy^{3+} channel in addition to the expected signal in the Ho^{3+} channel (Fig. 2b, c). Moreover, this anomalous signal in the Dy^{3+} channel increased significantly as the distance between the imaged $NaHoF_4$ LNPs and the $NaDyF_4$ layer decreased, increasing from <100 photons s^{-1} at a distance >100 μm to ≈12,000 photons s^{-1} at ≈5 μm from the $NaDyF_4$ edge. We attributed this behavior to the nonlocal excitation of the dense $NaDyF_4$ layer by stray electrons, which originated from the $NaHoF_4$ LNPs imaged with the primary electron beam. This hypothesis was supported by our Monte Carlo simulations, which confirmed that stray electrons from single LNPs could excite aggregates of LNPs located over 100 μm away from the imaged nanoparticle (Fig. 2d).

If stray electrons were indeed responsible for the nonlocal CL signal, then this signal should depend only on factors that influence the number of stray electrons, such as atomic number and sample topography. It should be independent of properties like the electronic structure of the imaged nanoparticles, which could hypothetically influence alternative mechanisms, such as locally enhancing substrate excitation or emitting photons that excite nearby LNPs—either of which could lead to increased energy transfer to the dense LNP layer. To test this hypothesis, we investigated nanoparticles with different electronic structures, including both lanthanide and non-lanthanide materials, i.e., $NaGdF_4$, $NaYF_4$, and 40-nm Au nanoparticles. The nanoparticles were imaged at different distances from a thick layer of $NaHoF_4$ LNPs, similar to Fig. 2a. In all cases we detected nonlocal CL signal from the $NaHoF_4$ layer upon excitation of sparse nanoparticles, with a similar distance-dependent trend as observed in Fig. 2c (Fig. 2e–g). This nonlocal signal primarily depended on the atomic number of the excited nanoparticles. For example, at 2 μm from the $NaHoF_4$ layer edge, we detected ≈55,000 photons s^{-1} from $NaGdF_4$, ≈80,000 photons s^{-1} from Au, and ≈20,000 photons s^{-1} from $NaYF_4$.

Next, we investigated the influence of substrate type on the nonlocal signal by testing two more substrates, Si_3N_4 (an insulator), and 80:20 Pt:Pd (a metal), in addition to Si (a semiconductor). For these experiments, we used a thick layer of $NaHoF_4$ and imaged sparse $NaGdF_4$ LNPs at different distances from the layer edge. Again, we consistently observed nonlocal CL signal from the layer across all substrate types (Fig. 2e, h, i). The signal strength depended on the difference in atomic number between the substrate and the excited LNP, with a larger difference leading to a higher apparent signal from the LNP. For instance, we detected on average ≈50,000 photons s^{-1} on Si_3N_4, when 2 μm away from $NaHoF_4$ layer (Fig. 2h), compared to ≈28,000 photons s^{-1} on the 80:20 Pt:Pd substrate (Fig. 2i).

Interestingly, on the 80:20 Pt:Pd substrate, we observed a shadow in the CL signal of the substrate, always adjacent to a sparse LNP and oriented such that the LNP was between the shadow and the dense layer (i.e., the shadow was behind the LNP) (Fig. 2j, Supplementary Fig. 14e). We observed this shadow behind LNPs when they were

https://doi.org/10.1038/s41467-025-64409-8

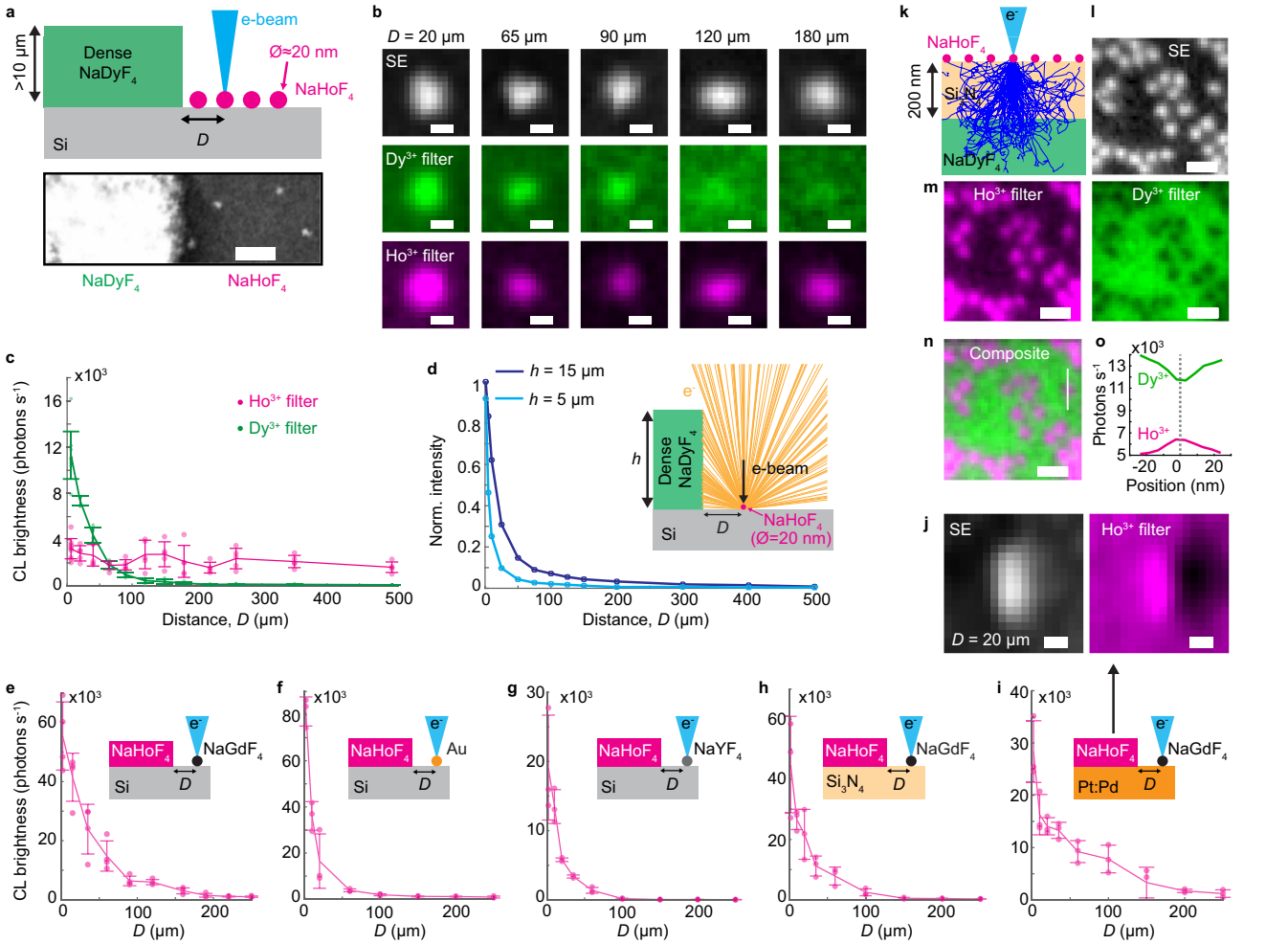

Fig. 2 | Nonlocal excitation limits multicolor single-particle imaging. a A schematic (not to scale) and SE image of a dense layer of $NaDyF_4$ LNPs and sparse $NaHoF_4$ LNPs on Si. **b** SE and CL images of $NaHoF_4$ LNPs at distances, *D*, from the $NaDyF_4$ layer. **c** CL brightness of single $NaHoF_4$ LNPs in Ho^{3+} and Dy^{3+} channels as a function of *D*. At least five LNPs 15–35 nm in diameter were imaged at each *D*. **d** Electron trajectory simulations of energy absorbed by a layer of $NaDyF_4$ LNPs upon excitation of a 20 nm-diameter $NaHoF_4$ LNP as a function of *D*. **e**–**i** CL brightness of single nanoparticles in the Ho^{3+} channel at distances, *D*, from a dense layer of $NaHoF_4$ LNPs. The subpanels show nanoparticle and substrate types. Three nanoparticles were imaged at each *D*. Diameters of sparse nanoparticles were 15–35 nm in (**e**, **g**, **h**, **i**) and 40 nm in (**f**). **j** SE and CL images of a $NaGdF_4$ LNP at $D = 20$ μm from the $NaHoF_4$ layer on Pt:Pd substrate. Note the shadow behind the LNP (right side). **k** Sample geometry for imaging $NaHoF_4$ LNPs on a 200-nm-thick Si_3N_4 window, with a dense layer of $NaDyF_4$ LNPs on the other side. Simulated electron trajectories for a beam energy of 5 keV are also shown. The top surface was coated with a 5-nm-thick layer of 80:20 Pt:Pd (not shown) to reduce charging artifacts. **l** SE and **m** CL images of $NaHoF_4$ LNPs for the geometry in (**k**). **n** Composite image of Ho^{3+} and Dy^{3+} channels from (**m**). **o** Cross-sectional profile of the LNP marked in (**n**). Scale bars: **a** 200 nm, **b**, **j** 20 nm, **l**–**n** 50 nm. Pixel intensity scaling across filters: **b** Ho^{3+}: 400–3000 photons s^{-1} (all *D*); Dy^{3+}: 2000–11,000 ($D = 20$ μm); 400–4000 ($D = 65$ μm); 400–1000 ($D = 90$ μm); 100–1080 ($D = 120$ μm); 100–1080 photons s^{-1} ($D = 180$ μm). **j** Ho^{3+}: 70,000–110,000 photons s^{-1}. Error bars in **c**, **e**–**i** show mean and standard deviation. Source data are provided as a Source Data file.

imaged up to ≈100 μm away from the dense $NaHoF_4$ layer. We attributed this effect to LNPs blocking stray electrons originating from the high-atomic-number substrate, thereby preventing them from reaching the dense layer. Such a reduction in nonlocal signal behind the LNPs was also predicted by Monte Carlo simulations of electron trajectories with a similar sample geometry (Supplementary Fig. 14f–h). Importantly, these simulations only modeled electron trajectories and did not include any other energy transfer mechanisms between the excited nanoparticle and the dense layer, which indicated that stray electrons alone were sufficient to account for the observed nonlocal effects. Together, these results confirmed that nonlocal excitation was not an intrinsic property of the Si substrate or the excited LNPs. Instead, it primarily depended on the atomic number of the substrate and the excited nanoparticle, which supported our hypothesis that stray electrons were the primary cause of the nonlocal signal (see Supplementary Figs. 9–14 for detailed discussion of nonlocal signal using different substrates and nanoparticles).

Furthermore, to rule out the possibility that photonic emission (e.g., X-rays or optical) from the excited nanoparticles were responsible for the nonlocal CL signal, we used a 200-nm layer of Si_3N_4 to separate a dense layer of $NaDyF_4$ nanocrystals and sparse $NaHoF_4$ LNPs. In this configuration, both the thick layer of $NaDyF_4$ and sparse $NaHoF_4$ LNPs were within the electron beam's interaction volume (Fig. 2k). However, when the beam was focused on $NaHoF_4$ LNPs, the electrons lost more energy when traversing the nanoparticles, compared to the substrate alone, which resulted in a reduced signal in the Dy^{3+} channel at the location of the Ho^{3+}-doped LNPs (Fig. 2l–o). This reduction showed that photonic emissions from excited LNPs, which could travel through the 200-nm Si_3N_4 layer (Supplementary Fig. 10), were not responsible for the nonlocal signal.

In summary, the stray electrons impacted typical EM samples of LNPs deposited on a Si substrate, which commonly contained both single, isolated LNPs and LNP aggregates. When a single LNP was imaged in such a sample, it served as a source of stray electrons, which

https://doi.org/10.1038/s41467-025-64409-8

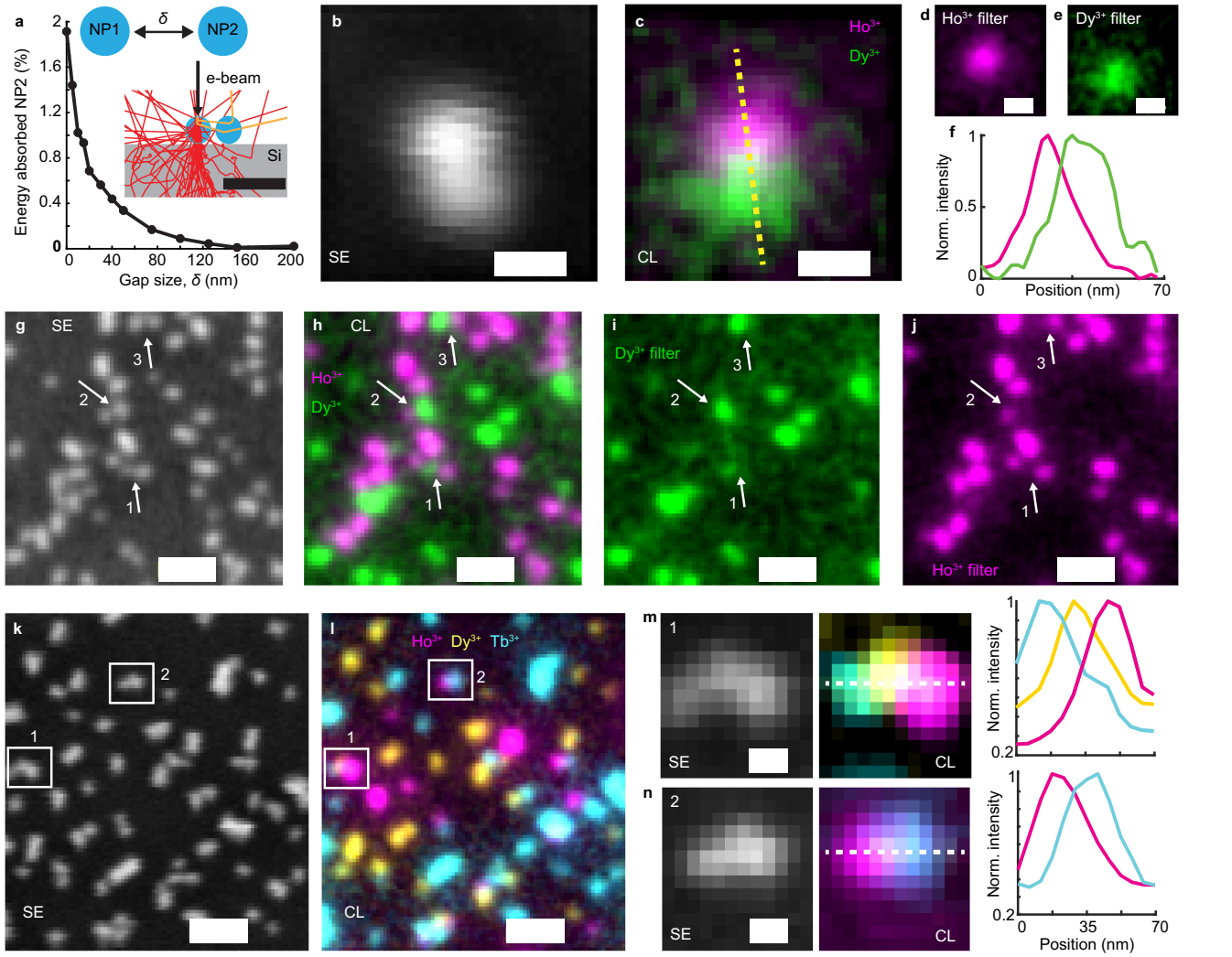

Fig. 3 | Multicolor single-particle CL imaging of spectrally distinct LNPs at the nanoscale. a Excitation crosstalk between two adjacent $NaHoF_4$ LNPs as analyzed by Monte Carlo simulations. Nanoparticle 1 (NP1) was excited with a 3 keV electron beam and the percentage of energy absorbed by NP2 (normalized to that of NP1) was calculated at different distances, δ, from NP1. 5000 trajectories were simulated at each distance, δ. Inset: Example of a simulation. **b** SE image of two LNPs located in direct proximity. **c** Composite CL image of the nanocrystals in (**b**), obtained by merging signals in **d** Ho^{3+} color channel and **e** Dy^{3+} color channel. **f** Cross-sectional profiles of the CL image along the dotted line shown in (**c**). **g** SE image of a field of view containing $NaHoF_4$ and $NaDyF_4$ LNPs. **h** Dual-color CL image of the field of view in (**g**), obtained by merging **i** Dy^{3+} color channel, and **j** Ho^{3+} color channel. Each LNP was detected in one of the two color channels, even when located close to nanocrystals of a different color; see arrows. **k** SE image of a field of view containing $NaHoF_4$, $NaDyF_4$, and $NaTbF_4$ LNPs. **l** Composite CL image of the field of view in (**k**) obtained by merging CL signals from Ho^{3+}, Dy^{3+}, and Tb^{3+} color channels. **m**, **n** Zoomed-in SE (left) and CL (right) images from regions indicated in (**k**, **l**), and CL cross-sectional profiles along the dotted lines in CL images. Scale bars: **a** 50 nm, **b**–**e** 20 nm, **g**–**l** 100 nm, **m**, **n** 20 nm. Pixel intensity scaling: **c**–**e** Dy^{3+} filter 400–700, Ho^{3+} filter: 300–1100 photons s^{-1}; **h**–**j** Dy^{3+} filter: 340–1000, Ho^{3+} filter: 700–4050 photons s^{-1}; **l** Tb^{3+} filter: 300–1100, Dy^{3+} filter: 440–1800, Ho^{3+} filter: 240–2400 photons s^{-1}; **m** Tb^{3+} filter: 300–600, Dy^{3+} filter: 520–1100, Ho^{3+} filter: 1200–2600 photons s^{-1}; **n** Tb^{3+} filter: 300–1000, Dy^{3+} filter: 520–1560, Ho^{3+} filter: 300–1600 photons s^{-1}. Source data are provided as a Source Data file.

in turn excited LNP aggregates in the field of view of the parabolic mirror (>100 µm, Supplementary Fig. 8). Because of this nonlocal electron excitation, the collected CL signal could contain contributions from LNP aggregates located tens of micrometers away from the LNP that was imaged with the primary electron beam. Interestingly, although the nonlocal CL signal appeared to originate from the spatial location of the imaged LNP, this was an artifact. This is because the heavy metal composition of the LNPs caused them to generate more stray electrons than the surrounding Si substrate (Supplementary Note 7, Supplementary Fig. 9). These electrons then traveled through free space and excited LNP aggregates located outside of the region imaged by the primary electron beam but within the field of view of the parabolic mirror. The result was the amplification of the nonlocal signal at the LNP's position.

Mitigating nonlocal excitation permits multicolor imaging

Having identified the origin and impact of the nonlocal CL signal, we investigated whether it would present a challenge for multicolor imaging in samples containing only single LNPs, i.e., in the absence of LNP aggregates. Such samples, while requiring careful preparation, are more suitable for studying CL imaging of single LNPs at the nanoscale. First, to determine whether the high density of single LNPs on the Si substrate would present a challenge in CL imaging, we performed Monte Carlo electron trajectory simulations to quantify the excitation crosstalk between two adjacent $NaHoF_4$ nanoparticles, each 20 nm in diameter (Fig. 3a). The simulations showed that when a single LNP was excited with the 3 keV electron beam, <2% of the total energy was deposited into the neighboring LNP, even if the two nanoparticles were in direct contact. Such minimal crosstalk suggested that multicolor CL

imaging with densely distributed but non-aggregated nanocrystals should be feasible.

To experimentally test this computational result, we optimized the sample preparation process to minimize LNP aggregation, achieving a 2D distribution of single LNPs on the Si wafer (Supplementary Note 2). Indeed, in such a sample, we were able to perform multicolor CL imaging with $NaHoF_4$ and $NaDyF_4$ LNPs in close proximity (Fig. 3b, c). Images of the LNPs in Ho^{3+} and Dy^{3+} color channels (Fig. 3d, e) and their cross-sectional profiles (Fig. 3f) show that the CL signal from the two nanoparticles was spatially separated, which allowed their spectral classification. Next, we imaged a larger field of view within a dense sample containing both $NaHoF_4$ and $NaDyF_4$ LNPs (Fig. 3g–j, Supplementary Fig. 16). Again, in this dense sample, we observed spectrally distinct CL from single LNPs in the same field of view. Each LNP was detected in only one of the two spectral channels, even when located just a few nanometers away from LNPs of a different spectral identity (Fig. 3b–f and arrows in Fig. 3g–j). Out of 54 nanoparticles in the image, 23 were classified as $NaDyF_4$ and the remaining 31 as $NaHoF_4$ (Supplementary Note 13, Supplementary Fig. 19).

We further extended the CL imaging to three colors using $NaHoF_4$, $NaDyF_4$, and $NaTbF_4$ LNPs (Fig. 3k–n, Supplementary Figs. 17, 18). These lanthanide ions were chosen because of their minimal spectral overlap. Figure 3k, l shows secondary electron (SE) and CL images of a field of view containing the three types of nanocrystals (see Supplementary Fig. 17 for individual spectral channels). Again, the LNPs emitted CL in spectrally distinct channels even when adjacent to LNPs of a different color (Fig. 3m, n). These results demonstrated the feasibility of multicolor single-particle CL imaging in densely populated samples of single LNPs.

The results presented in Fig. 3 demonstrated single-particle sensitivity in dense but non-aggregated samples. These observations, combined with the results presented in Fig. 2e–i, ruled out the alternative hypothesis that the nonlocal CL signal was caused by excitons diffusing in the Si substrate rather than stray electrons traveling through free space. If this nonlocal signal was caused by excitons, which may migrate over long distances (>100 μm) within the Si substrate[42], nonlocal CL signal would still be observed in samples of single LNPs distributed in 2D at high density. Instead, by reducing LNP aggregates, we minimized the combined surface area of LNPs upon which stray electrons could impinge and thereby excite CL (as illustrated in Fig. 2d inset).

Another unexpected source of nonlocal CL signal was the Everhart-Thornley secondary electron detector of the SEM, which uses a scintillator to detect incident electrons. We found that optical emission from the scintillator was reaching the CL detectors. Since LNPs generated more secondary electrons than the Si substrate, this led to increased scintillator emission and an artificially elevated CL signal at the LNP locations in the images. To mitigate this misleading signal, we reduced the bias voltage on the Everhart-Thornley detector, maintaining sufficient sensitivity for LNP imaging while minimizing its contribution to the nonlocal optical signal. In addition, we optically isolated the CL emission path within the vacuum chamber to prevent stray scintillator light, or any other nonlocal optical signal within the chamber, from reaching the CL detectors. Together, these improvements in CL instrumentation significantly reduced the nonlocal signal (Supplementary Note 26).

In summary, overcoming nonlocal excitation due to stray electrons was the key development that allowed us to achieve nanoscale, multicolor imaging of single LNPs in the same field of view. Nonlocal excitation could result in the apparent emission of single LNPs across multiple spectral channels. Therefore, demonstrating multicolor imaging of spectrally distinct LNPs in the same field of view was crucial in order to confirm single-particle detection capability. Conversely, single-color imaging alone was insufficient to establish single-particle detection sensitivity, even when the CL signal from LNPs spatially coincided with their image in the SE channel.

As described in the next section, achieving single-particle sensitivity not only permitted multicolor CL imaging but also enabled accurate single-particle characterization of CL emission from individual LNPs. In the presence of nonlocal CL signal, such measurements led to erroneous brightness values that did not scale monotonically with LNP size (Fig. 1b).

Characterization of CL emission in lanthanide nanocrystals

Next, we leveraged the single-particle sensitivity to determine the scaling of LNP brightness as a function of their diameter in the absence of nonlocal excitation. We defined CL brightness as photons detected per second from a nanoparticle (Methods, Supplementary Note 15). For these measurements, we used fully doped LNPs (i.e., $NaHoF_4$ or $NaDyF_4$) because they were within the brightness saturation regime with respect to dopant concentration (Supplementary Note 3, Supplementary Fig. 5). Specifically, LNP brightness plateaued for dopant concentrations above 20%, which we attributed to concentration quenching—where increased numbers of luminescent ions were offset by energy migration and cross-relaxation processes—as also observed in optically addressable LNPs[43]. Fully doped LNPs ensured consistent dopant concentration (100%), eliminating potential stoichiometric errors from mixing emitting and inert ions.

In addition, during CL imaging of single LNPs, image drift (a common phenomenon in EM[44]) posed a significant challenge due to the long acquisition times required to collect detectable CL signals from single LNPs, which only emitted a few hundred photons per second. To address the impact of image drift, we captured multiple images with shorter dwell times (e.g., 50 images at 1 ms pixel dwell time instead of a single image at 50 ms pixel dwell time) and applied drift correction post-acquisition using consecutive frames from SE imaging in which the single LNPs were visible even at short dwell times (Methods, Supplementary Note 15). This approach minimized the impact of image drift, allowing us to accurately determine LNP size and brightness. We then systematically varied the imaging conditions, such as beam current and beam energy, to optimize single-particle CL imaging (Supplementary Notes 17, 18).

For all dopants, LNP brightness increased monotonically with their diameter (Fig. 4a). In line with the prediction from Monte Carlo simulations, a linear fit was sufficient to describe the data, which suggested that LNP brightness was primarily dependent on their axial dimension. This linear relationship indicated a cylindrical shape of the electron interaction volume within LNPs of 15–30 nm diameter at a beam energy of 3 keV (Fig. 1c). We also compared linear and nonlinear (cubic and quadratic) fits for LNP brightness vs. size (Supplementary Note 21). Although these nonlinear fits did not improve the fit quality, the similar residual errors for the linear and nonlinear models suggested that higher-order dependencies could not be entirely ruled out, especially for larger nanoparticles. The linear model was chosen due to its simplicity and its agreement with the physical model suggested by simulations at a beam energy of 3 keV (Fig. 1c). Since we used the lateral dimensions of the LNPs to estimate their diameters, inhomogeneity in LNP dimensions may account for the observed variability in the CL signal for a given size, potentially reflecting differences in their axial dimensions. In addition, differences in electrobleaching between different LNPs (Supplementary Figs. 35, 36) could also contribute to the observed spread in the detected CL rate.

Figure 4a also shows that the CL brightness of LNPs depended on the type of lanthanide ion. For example, for a 20-nm $NaHoF_4$ nanoparticle we obtained ≈1100 photons s^{-1}, compared to ≈600 photons s^{-1} for $NaDyF_4$, ≈400 photons s^{-1} for $NaTbF_4$, and ≈250 photons s^{-1} for $NaSmF_4$. This dependency of CL brightness on the type of lanthanide ion could result from a combination of factors, including differences in absorption cross-sections, the percentage of emission concentrated in

https://doi.org/10.1038/s41467-025-64409-8

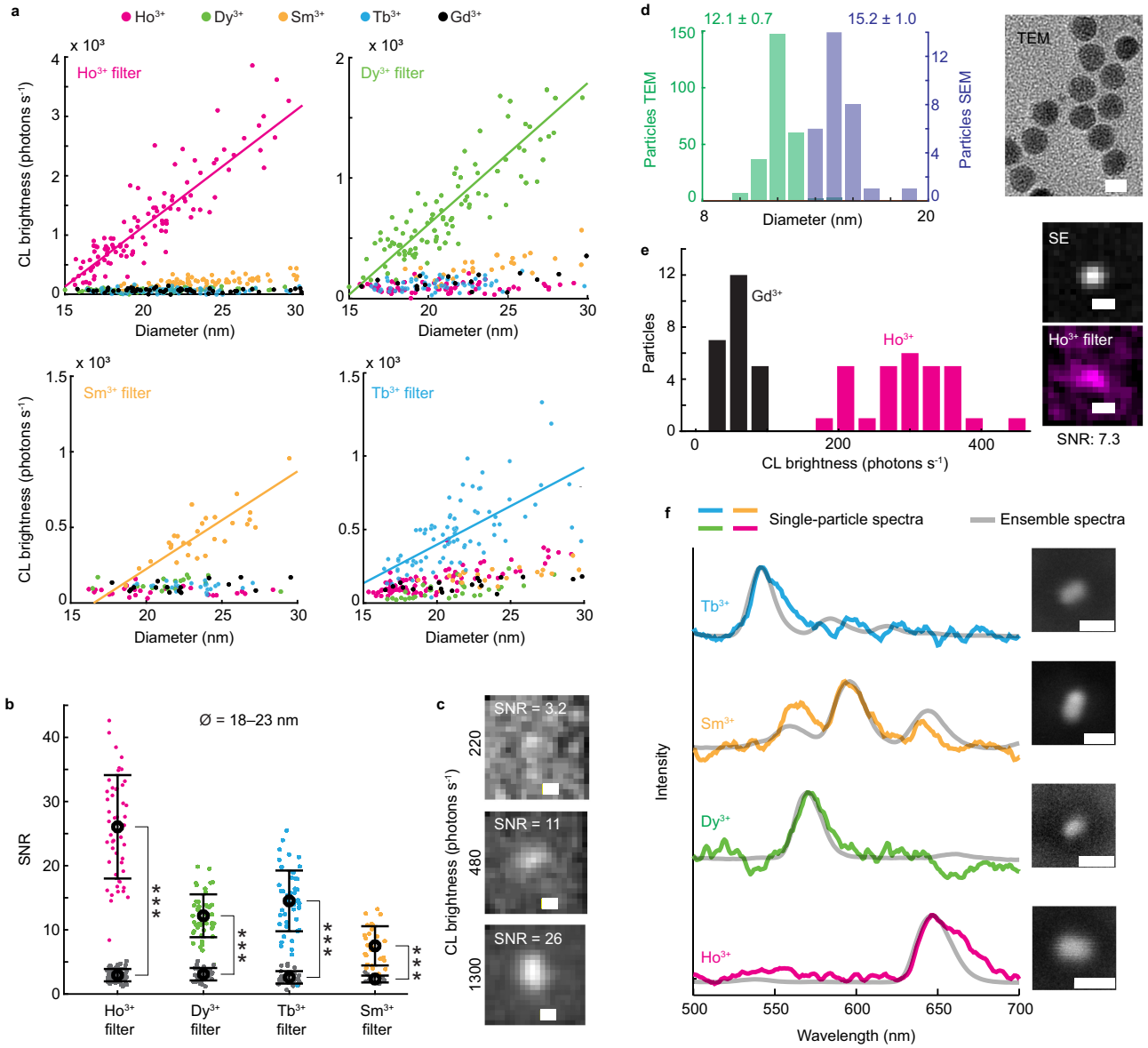

Fig. 4 | Characterization of single-particle CL emission. a CL photon detection rate as a function of diameter (full width at half maximum (FWHM) from SE images) for $NaHoF_4$, $NaDyF_4$, $NaSmF_4$, and $NaTbF_4$ LNPs across the spectral filters matched to their primary emission peaks. Linear fits to the CL signal as a function of diameter are also shown. CL signal from non-emitting control $NaGdF_4$ LNPs is shown as black dots. **b** SNR of CL images for $NaHoF_4$, $NaDyF_4$, $NaTbF_4$, and $NaSmF_4$ LNPs when imaged through their respective spectral filters. The number of single LNPs imaged was 52, 46, 51, and 27, respectively. SNR from control ($NaGdF_4$) LNPs is shown as gray dots. 56, 36, 31, and 11 $NaGdF_4$ LNPs were imaged in Ho^{3+}, Dy^{3+}, Tb^{3+}, and Sm^{3+} filters respectively. All LNPs were 18–23 nm in diameter. P-value was <0.001 (***) for all four LNP types in their respective filters. **c** Representative CL images with different SNRs. **d** Comparison of the nanocrystal size calculated using TEM (diameter of the circle fitted to nanocrystals) and SE (FWHM of the nanocrystals) images. A TEM image of nanocrystals is also shown. **e** Comparison of the CL detection rate from $NaHoF_4$ LNPs shown in (**d**) and control ($NaGdF_4$) LNPs. Representative SE and CL images of a $NaHoF_4$ LNP are also shown. **f** CL spectra of single LNPs (SE images on the right) and the corresponding ensemble spectra (gray). Scale bars: **c** 20 nm, **d** 10 nm, **e** 20 nm, **f** 50 nm. In (**a**) linear fits are of the form $r = mx + b$, where r is CL brightness in photons s^{-1}, x is the diameter of LNPs in nm, m is the slope in photons s^{-1} nm^{-1} and b is the y-intercept in photons s^{-1}. The fits are: Ho^{3+} filter: $r = 187x - 2607$ (from 165 LNPs), Dy^{3+} filter: $r = 117x - 1729$ (from 129 LNPs), Sm^{3+} filter: $r = 51x - 770$ (from 28 LNPs), and Tb^{3+} filter: $r = 47x - 543$ (from 83 LNPs). Error bars in **b** show mean and standard deviation. Source data are provided as a Source Data file.

the primary emission peak (e.g., 59% for Ho^{3+} and 40% for Sm^{3+}, Supplementary Fig. 7), excited state lifetimes, levels of electrobleaching (Supplementary Figs. 35,36), and quantum yields of different lanthanide ions.

The negative y-intercept for all dopants in Fig. 4a indicated a lower limit on the size of the smallest detectable LNPs in our system. The limit was primarily determined by the Poisson noise of the CL signal from Si substrate (Supplementary Note 19) because the LNPs were detected above this background signal (see Methods and Supplementary Note 15). For the four dopants, we detected sub-20-nm nanoparticles as shown in Fig. 4b, which shows a comparison of the signal-to-noise ratio (SNR) obtained from emitting LNPs with non-emitting control LNPs ($NaGdF_4$) in the same spectral channel.

To determine the required SNR for nanoparticle detection in CL images, we compared the SNR of emitting LNPs with that of the non-emitting control LNPs of the same size. We found that an SNR of ≈3 was sufficient to detect LNPs in all color channels (Supplementary Note 20 and Supplementary Fig. 31). A similar limit was calculated by modeling the Poisson noise in CL from Si, which yielded an SNR of 2.2, corresponding to a CL detection rate of ≈160 photons s^{-1} (Supplementary Fig. 30). Such

sensitive detection was possible because of the heavy metal composition of LNPs, which resulted in a strong contrast in SE images. This contrast allowed us to precisely localize individual nanoparticles and determine their diameters in SE images. This dual contrast (SE and CL images) provided CL imaging a key advantage over single-molecule localization microscopy, where the localization precision is dependent on the number of photons detected from a fluorophore[45].

LNP diameters were calculated from SE images, but due to their dependence on the electron beam diameter, we found that these calculations overestimated the actual LNP sizes. To exclude the effect of SEM resolution on the perceived size of the smallest detectable nanocrystals, we synthesized uniformly shaped nanocrystals of 12.1 ± 0.7 nm diameter (as determined by TEM), which were observed to be 15.2 ± 1.0 nm in our modified CL-SEM (Fig. 4d, Supplementary Fig. 4). These nanocrystals were consistently detected in CL images as shown in Fig. 4e, suggesting that we could detect nanocrystals at least as small as ≈12 nm. Therefore, the data in Fig. 4a overestimated the size of the smallest detectable nanoparticle.

Further improvements in the detection limit can be achieved by ensuring optimal excitation of LNPs, i.e., matching the electron interaction volume to the volume of the LNPs. However, matching the electron interaction volume to a 20-nm-diameter LNP required beam energies that were too low for our experimental setup (≈1 keV, Supplementary Figs. 26–28). This limitation was due to the long working distances required for CL imaging with the parabolic mirror installed between the electron gun and the sample. This microscope configuration resulted in deteriorated imaging performance in our SEM at low beam energies (Supplementary Fig. 27). Thus, we note that the LNPs were not excited optimally in our studies, suggesting opportunities for further signal maximization.

The spectral stability of single nanocrystals also played an important role in their color classification. We observed that the spectral characteristics of nanocrystals remained unchanged at the nanoscale by comparing their single-particle spectra to ensemble measurements (Fig. 4f, Supplementary Fig. 34). This spectral stability was crucial to match the optical filters to the main emission peaks of nanocrystals and thereby minimize the impact of broadband CL from the Si substrate (Supplementary Fig. 29). This observation highlights the utility of LNPs as nanoscale CL probes.

Multicolor single-particle CL imaging in a biological sample

After achieving single-particle sensitivity in CL measurements and characterizing the emission properties of LNPs on the Si substrate, we tested the sensitivity of our single-particle measurements in biological samples. Specifically, we sought to determine the emission characteristics of LNPs on the surface of a cultured mammalian cell. Here, a critical limitation was the auto-cathodoluminescence (auto-CL) from cells, which, by analogy with autofluorescence in fluorescence imaging, is the intrinsic luminescence of unlabeled cells excited with the electron beam[28,46]. Fixed HEK293T cells exhibited broadband auto-CL emission (Supplementary Fig. 37) and resulted in an average of ≈4300 and ≈2700 photons s^{-1} in Dy^{3+} and Ho^{3+} color channels, respectively (Fig. 5a). This auto-CL not only reduced the SNR of LNPs but also resulted in unexpected CL signal in multiple color channels due to nonlocal excitation of auto-CL when imaging the LNPs—an effect similar to the one presented in Fig. 2. We found that osmium tetroxide (OsO_4), a standard fixative and staining agent in EM sample preparation[47], reduced the auto-CL of cells (Fig. 5a). The auto-CL from OsO_4-treated cells was comparable to the background CL from the Si substrate, indicating that OsO_4 treatment was an effective chemical method for background auto-CL suppression.

We then measured CL from LNPs deposited on the surface of HEK293T cells prepared for standard SEM imaging (Fig. 5b, Supplementary Note 24). The sample preparation included OsO_4 treatment to mitigate auto-CL, and sputter coating with a 2.5-nm-thick 80:20 Pt:Pd mixture to avoid sample charging (Fig. 5c). Under these conditions, we observed an approximately two-fold reduction in the CL signal from the LNPs, which we attributed to their exposure to plasma during the sputter coating process. This hypothesis was supported by a similar reduction in the brightness of LNPs after exposure to plasma without sputter coating (Supplementary Fig. 39). On average, we collected ≈2500 photons s^{-1} from non-coated LNPs, compared to ≈1370 photons s^{-1} from sputter-coated LNPs on a Si substrate and ≈1450 photons s^{-1} from sputter-coated LNPs on cells. However, despite this reduced brightness, we collected sufficient photons to detect each imaged single sub-20 nm LNP. However, because LNP brightness scaled with size, this reduction in signal could limit the detectability of the smallest LNPs during CL imaging.

Finally, we performed multicolor imaging of $NaHoF_4$ and $NaDyF_4$ LNPs on the surface of HEK293T cells (Fig. 5d–g). Figure 5e shows that even after sputter coating, the LNPs produced a stronger contrast in SEM images than the cellular features. This contrast allowed for their precise localization in the SEM images, which was required for single-particle analysis. Similar to CL imaging on the Si substrate, the resolution in biological samples was determined by the size of the focused electron beam. However, we observed an increase in the effective size of the LNPs in sputter-coated samples due to the presence of the 2.5-nm-thick coating (Supplementary Fig. 38). Each LNP emitted CL in only one spectral channel, making it readily distinguishable. Importantly, both the nanoscale location and the spectral identity of each LNP, as well as the cellular ultrastructure, were visualized simultaneously.

These results demonstrate a proof of concept for multicolor single-particle CL imaging on the surface of a mammalian cell, with simultaneous visualization of cellular topography. Given the susceptibility of fluorescent dyes to quenching by EM sample preparation protocols[26], these findings highlight the photophysical stability of LNPs against the harsh chemical treatments required for EM sample preparation. Moreover, the sharp spectral features of lanthanide ions facilitated this multicolor single-particle imaging, as they allowed efficient spectral filtering to suppress any residual auto-CL after OsO_4 treatment. These findings were critical in establishing the suitability of LNPs for CL imaging in a biological context. Moreover, they highlight our ability to perform multicolor imaging in diverse systems.

Discussion

In conclusion, we identified nonlocal CL signals caused by stray electrons, generated due to strong beam-sample interaction in EM, as a critical limitation to achieving nanoscale multicolor CL imaging. Using lanthanide nanocrystals as a model system, selected because of their photostability under electron beam irradiation and availability in multiple emission colors, we systematically investigated the origin and impact of this nonlocal signal. We found that stray electrons could excite LNP aggregates located hundreds of micrometers away from the primary beam-sample interaction point. As a result, excitation of a single LNP could nonlocally excite multiple cathodoluminescent features within the sample. This nonlocal signal was difficult to distinguish from the true emission of the imaged LNP because LNPs were composed of heavier elements than the Si substrate and thereby produced more stray electrons. Since the total CL signal from the entire field of view of the parabolic mirror was collected at each scan position without spatial discrimination, the resulting nonlocal CL signal falsely appeared to be localized to the position of the LNP. These findings demonstrate that single-color CL imaging alone is insufficient to confirm single-particle sensitivity. To reliably establish single-particle detection sensitivity in both single and multicolor CL imaging, we identified two necessary conditions: a monotonic increase in CL rate as a function of LNP size, and multicolor single-particle imaging in the same field of view.

Identifying the origin of the nonlocal CL signal enabled us to develop the necessary strategies in sample preparation, instrumentation, imaging, spectroscopy, and image analysis to mitigate its impact

https://doi.org/10.1038/s41467-025-64409-8

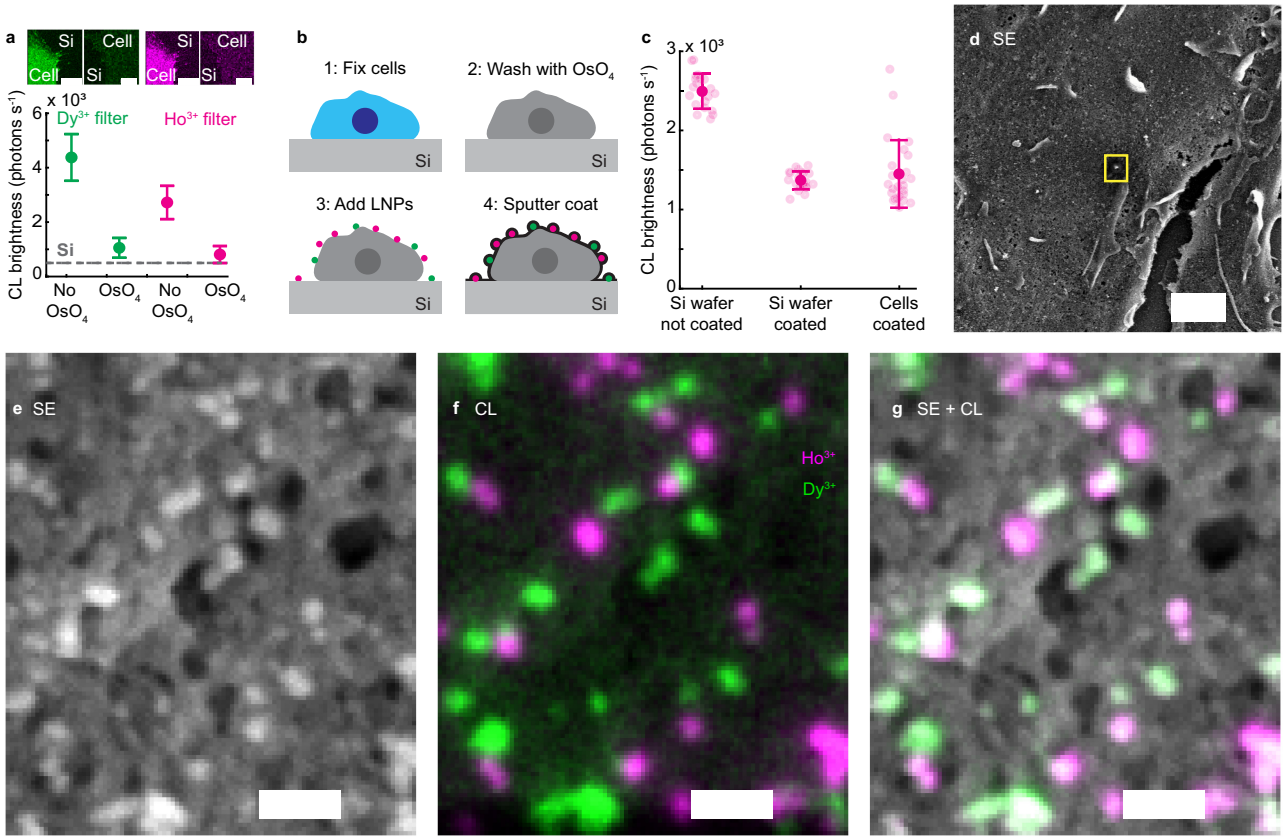

Fig. 5 | Multicolor single-particle CL imaging of LNPs in a biological sample. **a** Auto-CL photon detection rates from cells with and without OsO_4 treatment in Ho^{3+} and Dy^{3+} channels. Background CL from the Si substrate is also shown for comparison (dashed line). Five cells were imaged for each condition, and CL brightness was calculated from the pixels within the boundaries of all five cells. Boundaries were manually selected based on CL brightness of cells compared to background CL from Si (see top row). **b** An illustration showing the sample preparation procedure for imaging LNPs on cells. HEK293T cells were fixed, treated with OsO_4, and dried with hexamethyldisilazane (HMDS) (not shown in the illustration). LNPs were then drop-cast onto the cells. The biological sample with LNPs was sputter coated with 80:20 Pt:Pd mixture for SEM imaging. **c** CL detection rate in the Ho^{3+} channel from single $NaHoF_4$ LNPs on Si (with and without sputter coating) and on cells prepared for SEM imaging. Samples were prepared according to (**b**). The LNPs were 19.4 ± 0.6 nm in diameter, as measured in our CL-SEM. At least 20 LNPs were imaged for each condition. **d** SE image of a cell prepared according to (**b**) with $NaHoF_4$ and $NaDyF_4$ LNPs on the surface. **e**, **f** Zoomed-in SE (**e**) and CL (**f**) images of the region marked with a yellow rectangle in (**d**). **g** Merged image of the SE and CL channels. Pixel intensity in (**g**) is scaled differently from (**f**) to show only LNP signal above the background of cellular features. Scale bars: **a** 10 μm, **d** 1 μm, **e**–**g** 100 nm. Pixel intensity scaling: **f** Dy^{3+} filter 300–2000, Ho^{3+} filter: 300–6000 photons s^{-1}, and **g** Dy^{3+} filter 600–4000, Ho^{3+} filter: 1200–7000 photons s^{-1}. Error bars in **a**, **c** show the mean and standard deviation. Source data are provided as a Source Data file.

and consistently achieve multicolor, single-particle imaging. These developments included reducing nanoparticle aggregation in samples, eliminating nonlocal CL signal from the SEM components, and optimizing imaging parameters, including beam energy, current, and image acquisition times, as well as correcting for image drift. Leveraging these advancements, we demonstrated simultaneous CL imaging of multiple single nanocrystals of different emission colors within the same field of view. We also characterized the CL emission from individual nanocrystals, revealing a monotonic increase in CL signal as a function of nanoparticle size. Finally, we demonstrated multicolor imaging of LNPs in a biological sample, where they retained their emission throughout the EM sample preparation process. Through these advancements, we established a robust framework to harness the complete nanoscale, multicolor imaging potential of CL.

In the future, nanoscale CL imaging has the potential to be useful in a wide range of applications across disciplines. These may include investigating energy transfer between rare-earth ions and their emission in nanocrystals[5,48], as well as studying exciton and plasmon dynamics in diverse nanomaterials[49,50]. The localized optical excitation provided by CL can also be leveraged to excite individual color centers in crystals and single quantum dots—an important capability for the development of quantum light sources[51]. In bioimaging, CL presents a useful tool for obtaining molecular information along with the ultrastructural details (such as membranes and chromatin) provided by EM. The use of lanthanide nanocrystals as protein labels is promising in this regard due to their robust emission under electron excitation. This application of LNPs in molecular imaging will require surface functionalization to enable specific biomolecular targeting; existing functionalization strategies for optically addressable LNPs could serve as a starting point[52]. Our results will guide both the optimization of LNPs for protein labeling and the development of cathodoluminescent probes compatible with EM workflows. In addition, our findings on identifying and mitigating nonlocal excitation may also provide valuable insights for improving the spatial accuracy of other multicolor EM techniques, such as EDX. More broadly, our work provides a template for characterizing local nanoscale optical properties across diverse fields of science and engineering, offering a high-resolution, free-electron-based complement to photoluminescence.

Methods

Materials

Oleic acid (Sigma-Aldrich, Cat# 364525-1L, 90%, technical grade), 1-octadecene (SigmaAldrich, Cat# O806-1L, 90%, technical grade), rare-earth chlorides [yttrium trichloride hexahydrate (Sigma-Aldrich,

Cat# 464317-25G, 99.99%), samarium trichloride hexahydrate (Sigma-Aldrich, Cat# 204277-5G, ≥99.99%), gadolinium trichloride hexahydrate (Sigma-Aldrich, Cat# 203289-25G, 99.999%), terbium trichloride hexahydrate (Sigma-Aldrich, Cat# 212903-5G, 99.9%), dysprosium trichloride hexahydrate (Sigma-Aldrich, Cat# 289272-25G, 99.9%), holmium trichloride hexahydrate (Sigma-Aldrich, Cat# 289213-5G, 99.9%), lutetium trichloride hexahydrate (Sigma-Aldrich, Cat# 542075-5G, ≥99.99%)], sodium hydroxide (Sigma-Aldrich, Cat# 221465-500G, ACS Reagent, ≥97.0%, pellets), methanol (Sigma-Aldrich, Cat# 34860-1L-R, ≥99.9%), ammonium fluoride (Sigma-Aldrich, Cat# 216011-100G, ACS Reagent, ≥98.0%), n-hexane (Sigma-Aldrich, Cat# HX0302-3, 95%), ethanol (ethyl alcohol, Sigma-Aldrich, Cat# 459844-1L, ACS Reagent, ≥99.5%).

Nanoparticle synthesis

$NaHoF_4$, $NaDyF_4$, $NaTbF_4$, $NaSmF_4$, and $NaGdF_4$ LNPs were synthesized by the coprecipitation method based on refs. 28,53–55. Briefly, 0.5 mmol of the appropriate lanthanide chloride hydrate was mixed with 3 mL oleic acid and 7.5 mL 1-octadecene. The reaction was placed under vacuum, and the temperature was set to 160 °C for 30 min. The solution was cooled to <30 °C. Next, 1.25 mL of 1 M sodium hydroxide in methanol and 5 mL of 0.4 M ammonium fluoride in methanol were combined, then added to the lanthanide oleate solution. The reaction was mixed for 60 min at room temperature. The temperature was increased to 70 °C–80 °C and maintained for 30 min. Then, for the LNP growth step, the reaction was placed under an argon atmosphere and heated rapidly to 320 °C. The reaction temperature was maintained for 60 min before cooling to <30 °C. For uniformly shaped $NaHo_{0.8}Lu_{0.2}F_4$ LNPs, the synthesis was performed as described above, except that the 0.5 mmol of lanthanide chloride hydrates was divided into two quantities based on the desired molar ratio of the two lanthanide elements, and the 320 °C reaction temperature was maintained for 2.5 min (Fig. 4d) or 15 min (Fig. 5c), not 60 min, before cooling to <30 °C. LNPs were stored as-synthesized in oleic acid and 1-octadecene at room temperature.

Nanoparticle sample preparation

For single-particle experiments with minimal LNP aggregation, 0.5 mL of as-synthesized LNPs was mixed with 5 mL ethanol and centrifuged at 5000 × *g* for 10 min. The pellet was resuspended in 1 mL n-hexane, mixed with 5 mL ethanol, and centrifuged again. This process was repeated for a total of five times. After the fifth wash, the pellet was resuspended in 5 mL n-hexane, and the solution was left undisturbed overnight. For further sample preparation, LNP solution was pipetted from the top of the volume to avoid collecting precipitated LNP aggregates. The solution was drop-cast onto a TEM grid or an ethanol-washed and plasma-cleaned p-type Si wafer for characterization by TEM or SEM, respectively.

To obtain a solution of dense LNPs, 0.5 mL of as-synthesized LNPs was mixed with 0.5 mL ethanol and centrifuged at 3500 × *g* for 3 min. The pellet was resuspended in 0.5 mL n-hexane, mixed with 0.5 mL ethanol, and centrifuged again. This process was repeated for a total of five times. After the fifth wash, the pellet was resuspended in 0.5 mL n-hexane. The LNPs were used right away without settling overnight.

For experiments involving a dense nanocrystal region and a sparse nanocrystal region separated by a well-defined edge as presented in Fig. 2, a piece of ≈1 cm^2 Si was cut from a p-type Si wafer (Ted Pella, Cat# 16015). The piece was ethanol-washed and plasma-cleaned. Then, half of its surface was covered with tape (Scotch Magic Tape). 5 µL of dense, n-hexane-suspended nanocrystals were drop-cast onto the exposed half of the Si wafer's surface. After the n-hexane dried, drop-casting and drying were repeated four times to create a thick layer of dense nanocrystals. Finally, the tape was removed from the Si wafer's surface, the desired n-hexane-suspended single LNPs were diluted 100–1000× in n-hexane to achieve sparsity, and 5 µL was drop-cast onto the wafer.

CL imaging setup

Imaging was performed on a custom-modified ZEISS SUPRA 55VP FESEM, integrated with a CL imaging system. CL was collected by an off-axis, aluminum parabolic mirror with a collection solid angle of ≈1.34π steradian. The mirror had a focal length of 1 mm. The mirror directed CL out of the vacuum chamber of the SEM, where it was spectrally separated using dichroic mirrors, filtered by band-pass filters, and projected onto photomultiplier tubes (Hamamatsu, H7421-40) using 30 mm-focal-length lenses. CL was simultaneously collected over three color channels. The spectral filters were Chroma ET645/30X (Ho^{3+} color channel), Chroma FF03-575/25 (Dy^{3+} color channel), Semrock FF01-598/25 (Sm^{3+} color channel) and Chroma ET550/20X (Tb^{3+} color channel).

Spectral measurements

For single-particle spectra, a nanocrystal was repeatedly scanned with the electron beam. CL was collected by the parabolic mirror and focused on an sCMOS camera (Hamamatsu, Orca-Fusion BT) using a 100 mm focal length lens. A diffraction grating (Thorlabs, GT13-03) was placed before the camera to spectrally separate the CL signal. Spectra were obtained with a beam energy of 3 keV and a beam current of 200 pA. The spectral information resided in the first diffraction order of the grating. Spectra were obtained by plotting the intensity of pixels in the first diffraction order as a function of distance from the center of the zeroth order. All spectra presented in Fig. 4f were obtained using this method.

For spectra in Fig. 1a, a dense sample of nanocrystals was prepared. A 400 × 400 nm^2 region of the sample was repeatedly scanned with the electron beam. CL was collected by the parabolic mirror and focused on the multimode fiber of a commercial spectrometer (Thorlabs, CCS200). Spectra were obtained with a beam energy of 3 keV and a beam current of 200 pA.

CL image acquisition

Single-particle CL imaging was performed with an electron beam energy of 3 keV and a beam current of 160–200 pA. The working distance was 6–7 mm. Both the Zeiss SmartSEM software and custom LabVIEW software were used for image acquisition. A region of interest was imaged with a pixel size of 4–8 nm. Four images were captured during each scan of the electron beam: one SE image and three CL images in different spectral channels. CL images were smoothed by convolution with a 2D Gaussian function of 0.7 pixels standard deviation. To characterize emission properties of LNPs, 50 frames were captured with a dwell time of 1 ms each, resulting in an effective beam dwell time of 50 ms per pixel. These conditions translated to a current density of 3–12 pA per nm^2 and a total electron dose of ≈62.5×10^6 electrons per pixel. For multicolor experiments, images were acquired with a beam dwell time of 0.1–1 ms and an effective beam dwell time of 30–50 ms. For visualization, CL images presented in the paper were filtered with a 2D Gaussian function of 0.5–0.7 pixel standard deviation.

In Fig. 3l, 15% of the signal intensity in the Ho^{3+} channel was subtracted from the Tb^{3+} channel before generating the overlapped image. This was because the minor peak of $NaHoF_4$ LNPs overlapped with the Tb^{3+} filter (Supplementary Fig. 7e). The factor was calculated based on the ratio of the emission of $NaHoF_4$ LNPs in the Ho^{3+} and Tb^{3+} channels.

For experiments to quantify nonlocal excitation presented in Fig. 2, 3–5 LNPs were imaged at fixed distances from the edge. Since the dense LNPs were not necessarily distributed in a well-defined, straight line along the edge, the distance was measured relative to a consistent point at the edge between the dense layer of LNPs and the sparse LNPs.

Drift correction

Drift correction was performed by acquiring multiple sequential frames using a short dwell time, instead of a single image with a long dwell time. Nanocrystals themselves were used as fiducial markers in SE images. The position of a nanocrystal was determined by fitting a 2D Gaussian function to its SE image. Euclidean distance between the positions of the nanocrystal in successive SE frames was calculated and rounded to the nearest integer. This distance was then used to translate SE and CL images to account for the drift during image acquisition.

CL emission rate and photons per frame

CL properties of a nanocrystal were determined by first localizing it in the SE images and then determining its emission properties at the corresponding location in the CL images. The position of the nanocrystal in an SE image was determined by fitting a 2D Gaussian function. The CL image was then fit to a 2D Gaussian function of the form:

$$S(x,y) = b + a\exp\left[-\frac{(x-x_0)^2}{2\sigma_x^2} - \frac{(y-y_0)^2}{2\sigma_y^2}\right] = b + G(x,y)$$

where (x_0, y_0) is the center position of the nanocrystal, b is the background, a is amplitude, and σ_x and σ_y are the standard deviations of the 2D Gaussian function. $G(x,y)$ is the 2D Gaussian fit to the nanocrystal without the background. In this equation, x_0, y_0, σ_x, and σ_y were constrained by the 2D Gaussian fit of the SE image. The rate of CL emission was determined as $r = \frac{a}{\mathrm{dt}} \times 1,000$, and the total number of photons emitted by the nanocrystal in a frame was calculated by summing over $G(x,y)$.

SNR analysis

SNR of a nanocrystal in a CL image was determined using the equation S/N, where S corresponds to the summation over $G(x,y)$, i.e., $S = \sum G(x,y)$. Only pixels within a 2σ radius from the center of the Gaussian fit were considered. The noise, N_i, for pixel (x,y) was calculated as $\sqrt{I(x,y)}$, where $I(x,y)$ is the CL intensity of that pixel. To determine the overall noise, N, the per-pixel noise, N_i, was added in quadrature over the pixels within a 2σ radius from the center of the nanocrystal as $N = \sqrt{\sum N_i^2} = \sqrt{\sum I(x,y)}$. Hence, the overall SNR for a single nanocrystal was given by $\frac{S}{N} = \frac{\sum G(x,y)}{\sqrt{\sum I(x,y)}}$.

Size of the nanocrystal

The diameter (also referred to as size) of a nanocrystal was determined from the oversampled SE images taken with the ZEISS SmartSEM software (pixel size 0.2–0.6 nm). To determine the diameter of a nanocrystal, a 2D Gaussian function was fitted to its SE image. Diameter was defined as the FWHM of this fit. FWHM was calculated from the standard deviation of the Gaussian fit as 2.35σ. Here σ is the average of the two standard deviations (σ_x and σ_y) of the 2D Gaussian fit.

Statistical significance

In Fig. 4b, the P-value was calculated using Welch's two-sample t-test, with the null hypothesis that the SNR from emitting ($NaHoF_4$, $NaDyF_4$, $NaTbF_4$, and $NaSmF_4$) and control ($NaGdF_4$) LNPs were drawn from independent normal distributions with equal means. The test was performed in MATLAB using the ttest2 function with unequal variances for the two distributions.

Electron trajectory simulations

CASINO software[56] was used to perform Monte Carlo-based electron trajectory simulations. Nanoparticles were simulated using the sphere object with 20 nm diameter. The Si substrate, Si_3N_4 substrate, and dense layer of nanoparticles were simulated using the box object. In Fig. 2d, 20,000 trajectories were simulated with a beam energy of 3 keV. In Fig. 2k, 20,000 trajectories were simulated (only 100 are shown) with a beam energy of 5 keV. In Fig. 3a, 50,000 trajectories were simulated with a beam energy of 3 keV.

Biological sample preparation

Cultured cells were prepared for CL imaging via OsO_4 treatment and HMDS drying based on refs. 57,58. HEK293T cells were cultured in 50/50 DMEM/F-12 media with 10% fetal bovine serum and 1% penicillin/streptomycin. Cells were dissociated using 0.25% trypsin in PBS, then seeded on plasma-cleaned Si wafers. After adhering to Si overnight, cells were washed twice with PBS and fixed with 4% formaldehyde, 0.2% glutaraldehyde in PBS, pH 7.4 for 15 min. Cells were washed three times with PBS and incubated in 1% OsO_4 in PBS for 10 min. Then, cells were washed with MilliQ water for 2 h, replacing water every 15 min. Cells were transitioned into ethanol by increasing from 10% ethanol to 100% ethanol using steps of 10%, with 5 min between each step. Upon reaching 100% ethanol, cells were incubated twice for 20 min with fresh ethanol each time. Next, cells were transitioned into HMDS by increasing from 25% HMDS in ethanol to 100% HMDS using steps of 25%, with 5 min between each step. When 100% HMDS was reached, cells were incubated twice for 20 min with fresh HMDS each time. Finally, the majority of HMDS volume was removed from the cells to leave a thin layer of HMDS, and cells were air dried. If appropriate, 5 µL of washed, n-hexane-suspended single LNPs was drop-cast onto the cells. Finally, cells were sputter coated with a 2.5-nm-thick layer of 80:20 Pt:Pd to prevent charging during CL-SEM imaging.

Data availability

The data that support the findings of this study are available from the corresponding author upon request. A preprint has been deposited at bioRxiv[59]. Source data are provided with this paper.

References

1. Grimm, J. B. & Lavis, L. D. Caveat fluorophore: an insiders' guide to small-molecule fluorescent labels. *Nat. Methods* **19**, 149–158 (2022).
2. Grimm, J. B., Heckman, L. M. & Lavis, L. D. The chemistry of small-molecule fluorogenic probes. *Prog. Mol. Biol. Transl. Sci.* **113**, 1–34 (2013).
3. Costantini, L. M. et al. A palette of fluorescent proteins optimized for diverse cellular environments. *Nat. Commun.* **6**, 7670 (2015).
4. Bovensiepen, U. & Kirchmann, P. S. Elementary relaxation processes investigated by femtosecond photoelectron spectroscopy of two-dimensional materials. *Laser Photon. Rev.* **6**, 589–606 (2012).
5. Teitelboim, A. et al. Energy transfer networks within upconverting nanoparticles are complex systems with collective, robust, and history-dependent dynamics. *J. Phys. Chem. C Nanomater. Interfaces* **123**, 2678–2689 (2019).
6. Menke, S. M. & Holmes, R. J. Exciton diffusion in organic photovoltaic cells. *Energy Environ. Sci.* **7**, 499–512 (2014).
7. Pfeifer, T., Kütt, W., Kurz, H. & Scholz, R. Generation and detection of coherent optical phonons in germanium. *Phys. Rev. Lett.* **69**, 3248–3251 (1992).
8. Wang, L., Hasanzadeh Kafshgari, M. & Meunier, M. Optical properties and applications of plasmonic-metal nanoparticles. *Adv. Funct. Mater.* **30**, 2005400 (2020).
9. Zhou, L. et al. Nonlinear optical characterization of 2D materials. *Nanomaterials* **10**, 2263 (2020).
10. Betzig, E. & Trautman, J. K. Near-field optics: microscopy, spectroscopy, and surface modification beyond the diffraction limit. *Science* **257**, 189–195 (1992).
11. Betzig, E. et al. Imaging intracellular fluorescent proteins at nanometer resolution. *Science* **313**, 1642–1645 (2006).

12. Rust, M. J., Bates, M. & Zhuang, X. Sub-diffraction-limit imaging by stochastic optical reconstruction microscopy (STORM). *Nat. Methods* **3**, 793–795 (2006).
13. Hell, S. W. & Wichmann, J. Breaking the diffraction resolution limit by stimulated emission: stimulated-emission-depletion fluorescence microscopy. *Opt. Lett.* **19**, 780–782 (1994).
14. Balzarotti, F. et al. Nanometer resolution imaging and tracking of fluorescent molecules with minimal photon fluxes. *Science* **355**, 606–612 (2017).
15. Hell, S. W. Far-field optical nanoscopy. *Science* **316**, 1153–1158 (2007).
16. García de Abajo, F. J. Optical excitations in electron microscopy. *Rev. Mod. Phys.* **82**, 209–275 (2010).
17. Scimeca, M., Bischetti, S., Lamsira, H. K., Bonfiglio, R. & Bonanno, E. Energy dispersive X-ray (EDX) microanalysis: a powerful tool in biomedical research and diagnosis. *Eur. J. Histochem.* **62**, 2841 (2018).
18. Colliex, C. From early to present and future achievements of EELS in the TEM. *Eur. Phys. J. Appl. Phys.* **97**, 38 (2022).
19. Varkentina, N. et al. Cathodoluminescence excitation spectroscopy: nanoscale imaging of excitation pathways. *Sci. Adv.* **8**, eabq4947 (2022).
20. Kociak, M. & Zagonel, L. F. Cathodoluminescence in the scanning transmission electron microscope. *Ultramicroscopy* **176**, 112–131 (2017).
21. Guthrey, H. & Moseley, J. A review and perspective on cathodoluminescence analysis of Halide perovskites. *Adv. Energy Mater.* **10**, 1903840 (2020).
22. Mahfoud, Z. et al. Cathodoluminescence in a scanning transmission electron microscope: a nanometer-scale counterpart of photoluminescence for the study of II–VI quantum dots. *J. Phys. Chem. Lett.* **4**, 4090–4094 (2013).
23. Meuret, S. et al. Photon bunching reveals single-electron cathodoluminescence excitation efficiency in InGaN quantum wells. *Phys. Rev. B Condens. Matter* **96**, 035308 (2017).
24. Kim, Y.-J. & Kwon, O.-H. Cathodoluminescence in ultrafast electron microscopy. *ACS Nano* **15**, 19480–19489 (2021).
25. *Cathodoluminescence in Geosciences*. (Springer, 2000).
26. de Boer, P., Hoogenboom, J. P. & Giepmans, B. N. G. Correlated light and electron microscopy: ultrastructure lights up!. *Nat. Methods* **12**, 503–513 (2015).
27. Keevend, K., Coenen, T. & Herrmann, I. K. Correlative cathodoluminescence electron microscopy bioimaging: towards single protein labelling with ultrastructural context. *Nanoscale* **12**, 15588–15603 (2020).
28. Prigozhin, M. B. et al. Bright sub-20-nm cathodoluminescent nanoprobes for electron microscopy. *Nat. Nanotechnol.* **14**, 420–425 (2019).
29. Wu, S. et al. Non-blinking and photostable upconverted luminescence from single lanthanide-doped nanocrystals. *Proc. Natl. Acad. Sci. USA* **106**, 10917–10921 (2009).
30. Sun, L.-D., Dong, H., Zhang, P.-Z. & Yan, C.-H. Upconversion of rare earth nanomaterials. *Annu. Rev. Phys. Chem.* **66**, 619–642 (2015).
31. Glenn, D. R. et al. Correlative light and electron microscopy using cathodoluminescence from nanoparticles with distinguishable colours. *Sci. Rep.* **2**, 865 (2012).
32. Keevend, K. et al. Ultrabright and stable luminescent labels for correlative cathodoluminescence electron microscopy bioimaging. *Nano Lett.* **19**, 6013–6018 (2019).
33. Keevend, K. et al. Correlative cathodoluminescence electron microscopy: immunolabeling using rare-earth element doped nanoparticles. *Small* **16**, e2004615 (2020).
34. Swearer, D. F. et al. Single particle cathodoluminescence spectroscopy with sub-20 nm, electron-stable phosphors. *ACS Photonics* **8**, 1539–1547 (2021).
35. Habermann, S. et al. Cathodoluminescent and characteristic X-ray-emissive rare-earth-doped core/shell protein labels for spectro-microscopic analysis of cell surface receptors. *Small* **20**, e2404309 (2024).
36. Niioka, H. et al. Multicolor cathodoluminescence microscopy for biological imaging with nanophosphors. *Appl. Phys. Express* **4**, 112402 (2011).
37. Garming, M. W. H. et al. Nanoparticle discrimination based on wavelength and lifetime-multiplexed cathodoluminescence microscopy. *Nanoscale* **9**, 12727–12734 (2017).
38. Furukawa, T. et al. Rare-earth-doped nanophosphors for multicolor cathodoluminescence nanobioimaging using scanning transmission electron microscopy. *J. Biomed. Opt.* **20**, 056007 (2015).
39. Ren, P. et al. Quantifying the influence of inert shell coating on luminescence brightness of lanthanide upconversion nanoparticles. *ACS Photonics* **9**, 758–764 (2022).
40. Wang, F., Wang, J. & Liu, X. Direct evidence of a surface quenching effect on size-dependent luminescence of upconversion nanoparticles. *Angew. Chem. Int. Ed. Engl.* **49**, 7456–7460 (2010).
41. Toth, M. & Phillips, M. R. Monte Carlo modeling of cathodoluminescence generation using electron energy loss curves. *Scanning* **20**, 425–432 (1998).
42. Saritas, M. & McKell, H. D. Comparison of minority-carrier diffusion length measurements in silicon by the photoconductive decay and surface photovoltage methods. *J. Appl. Phys.* **63**, 4561–4567 (1988).
43. Wang, Z. & Meijerink, A. Concentration quenching in upconversion nanocrystals. *J. Phys. Chem. C. Nanomater. Interfaces* **122**, 26298–26306 (2018).
44. Marturi, N., Dembele, S. & Piat, N. Fast image drift compensation in scanning electron microscope using image registration. In *Proc. IEEE International Conference on Automation Science and Engineering (CASE)*. https://doi.org/10.1109/coase.2013.6653936 (IEEE, 2013).
45. Thompson, R. E., Larson, D. R. & Webb, W. W. Precise nanometer localization analysis for individual fluorescent probes. *Biophys. J.* **82**, 2775–2783 (2002).
46. Zielinski, M. S. et al. Quantitative intrinsic auto-cathodoluminescence can resolve spectral signatures of tissue-isolated collagen extracellular matrix. *Commun. Biol.* **2**, 69 (2019).
47. Tapia, J. C. et al. High-contrast en bloc staining of neuronal tissue for field emission scanning electron microscopy. *Nat. Protoc.* **7**, 193–206 (2012).
48. Bünzli, J.-C. G. & Piguet, C. Taking advantage of luminescent lanthanide ions. *Chem. Soc. Rev.* **34**, 1048–1077 (2005).
49. Wheeler, D. A. & Zhang, J. Z. Exciton dynamics in semiconductor nanocrystals. *Adv. Mater.* **25**, 2878–2896 (2013).
50. Linic, S., Chavez, S. & Elias, R. Flow and extraction of energy and charge carriers in hybrid plasmonic nanostructures. *Nat. Mater.* **20**, 916–924 (2021).
51. Ma, J. et al. Engineering quantum light sources with flat optics. *Adv. Mater.* **36**, e2313589 (2024).
52. Li, L.-L., Wu, P., Hwang, K. & Lu, Y. An exceptionally simple strategy for DNA-functionalized up-conversion nanoparticles as biocompatible agents for nanoassembly, DNA delivery, and imaging. *J. Am. Chem. Soc.* **135**, 2411–2414 (2013).
53. Fischer, S., Bronstein, N. D., Swabeck, J. K., Chan, E. M. & Alivisatos, A. P. Precise tuning of surface quenching for luminescence enhancement in core–shell lanthanide-doped nanocrystals. *Nano Lett.* **16**, 7241–7247 (2016).
54. Wang, F., Deng, R. & Liu, X. Preparation of core-shell NaGdF4 nanoparticles doped with luminescent lanthanide ions to be used as upconversion-based probes. *Nat. Protoc.* **9**, 1634–1644 (2014).
55. Shang, Y. et al. Low threshold lasing emissions from a single upconversion nanocrystal. *Nat. Commun.* **11**, 6156 (2020).

56. Drouin, D. et al. CASINO V2.42: a fast and easy-to-use modeling tool for scanning electron microscopy and microanalysis users. *Scanning* **29**, 92–101 (2007).
57. Tanida, I. et al. Two-color in-resin CLEM of Epon-embedded cells using osmium resistant green and red fluorescent proteins. *Sci. Rep.* **10**, 21871 (2020).
58. Schu, M. et al. Scanning electron microscopy preparation of the cellular actin cortex: a quantitative comparison between critical point drying and hexamethyldisilazane drying. *PLoS One* **16**, e0254165 (2021).
59. Abdul Rehman, S. et al. Lanthanide cathodophores for multicolor electron microscopy. *bioRxiv*, https://doi.org/10.1101/2023.12.11.570835 (2023).

Acknowledgements

This work was supported by the Scialog Award from the Gordon and Betty Moore Foundation (M.B.P.), the Aramont Fellowship Fund for Emerging Science Research (M.B.P.), NIH grant R01GM146791 (M.B.P.), NIH grant R21GM146127 (M.B.P.), NIH grant R01NS134846 (M.B.P.), and startup funds from Harvard University (M.B.P.). J.B.C. was supported in part by the Harvard QBio Student Award. A.D. and I.M. were supported by the Harvard Systems Biology Internship Program. Harvard QBio and the Harvard Systems Biology Internship Program are supported by the NSF-Simons Center for the Mathematical & Statistical Analysis of Biology at Harvard University. K.S. was supported by the Harvard MCO SROH Internship Program and The Leadership Alliance's Summer Research Early Identification Program. Part of this work was performed at the Harvard University Center for Nanoscale Systems (CNS), a member of the National Nanotechnology Coordinated Infrastructure Network (NNCI), which is supported by the National Science Foundation under NSF award no. ECCS-2025158. The authors thank Arvind Srinivasan, Ami Thakrar, Daphne-Eleni Archonta, Balmiki Kumar, and Ethan Garner for useful discussions, as well as James MacArthur for assistance with CL instrumentation. The authors are grateful to Adam Cohen, Rachelle Gaudet, Martin Gruebele, Prashant Jain, Catherine Murphy, Daniel Needleman, Bridget Queenan and Ariane Vertanian for critical reading of the manuscript.

Author contributions

S.A.R., J.B.C., and M.B.P. conceived the project, designed experiments, analyzed the data, and interpreted the results. S.A.R. developed the CL detection system and implemented the hardware-software integration for simultaneous SEM and CL imaging. S.A.R. developed the imaging and data analysis pipeline. S.A.R. and J.B.C. performed CL imaging. J.B.C. optimized the nanoparticle synthesis protocol. J.B.C. performed TEM imaging. S.A.R., J.B.C., A.N., K.S., and I.M. synthesized nanoparticles. E.R.S. assisted with implementing automated electron beam scanning. S.A.R. and A.D. performed Monte Carlo simulations of electron trajectories. S.M. developed the probabilistic classification framework and analysis methods for color assignment in multicolor images. S.A.R., J.B.C., A.N., K.S., I.M., and A.C. prepared nanoparticles for imaging. J.B.C. performed cell culture and optimized the biological sample preparation protocol for CL imaging. S.A.R., J.B.C., and M.B.P. wrote the manuscript. M.B.P. supervised the research.

Competing interests

The authors declare no competing interests.

Additional information

Supplementary information The online version contains supplementary material available at https://doi.org/10.1038/s41467-025-64409-8.

Correspondence and requests for materials should be addressed to Maxim B. Prigozhin.

Peer review information *Nature Communications* thanks Oh-Hoon Kwon and the other anonymous reviewer(s) for their contribution to the peer review of this work. A peer review file is available.